lubricants

MDPI

Article

Coupled Model of Point-Contact Thermo-Elastohydrodynamic Lubrication and Dynamics with Double-Impact Mechanism for High-Precision Quantitative Diagnosis of Rolling Bearings

Wei Jin [1,2], Chao Liu [1], Tongtong Liu [1,*], Jinfeng Huang [3], Chengshi Zhang [1], Feng Jin [4], Feibin Zhang [3] and Chao Zhang [1]

[1] Inner Mongolia Key Laboratory of Intelligent Diagnosis and Control of Mechatronic System, Inner Mongolia University of Science and Technology, Baotou 014010, China
[2] Department of Chemical and Materials Engineering, Baotou Light Industry Vocational Technical College, Baotou 014035, China
[3] State Key Laboratory of Tribology, Department of Mechanical Engineering, Tsinghua University, Beijing 100080, China
[4] Inner Mongolia Institute of Special Equipment Inspection and Research, Energy Equipment Intelligent Inspection and Safety Assurance Laboratory, Baotou 010020, China
* Correspondence: liuzhaishi@imust.edu.cn

Abstract

Accurate quantitative diagnosis of spall sizes in rolling bearings is often hindered by the limitations of conventional dynamic models in characterizing temperature-dependent contact behavior. To address this issue, this paper presents a quantitative diagnosis method that incorporates point-contact thermo-elastohydrodynamic lubrication (TEHL) characteristics into a classical bearing dynamic framework. Specifically, rather than using prescribed or constant contact parameters, an improved equivalent stiffness–damping representation of the bearing contact interface is formulated based on TEHL-derived oil-film pressure, thickness, and temperature, while taking into account the inner–outer raceway thermal asymmetry. This localized lubricated contact representation is subsequently integrated into a classical five-degree-of-freedom (5-DOF) dynamic model to evaluate the double-impact response caused by outer-ring spalls. Comparative simulations using conventional 5-DOF, 4-DOF, and 2-DOF models, alongside experiments on a 6205-2-RS bearing with a 0.6 mm outer-ring defect, validate the proposed method. The results demonstrate that utilizing the TEHL-derived stiffness–damping representation significantly reduces spall-size estimation errors, improving both the accuracy and the physical interpretability of bearing fault quantification under thermally coupled conditions.

Keywords: rolling bearing; thermo-elastohydrodynamic lubrication; dynamic modeling; quantitative diagnosis

Check for updates

Received: 20 May 2026
Revised: 24 June 2026
Accepted: 26 June 2026
Published: 30 June 2026

Copyright: © 2026 by the authors. Licensee MDPI, Basel, Switzerland. This article is an open access article distributed under the terms and conditions of the Creative Commons Attribution (CC BY) license.

1. Introduction

Rolling bearings are key supporting components in rotating machinery, and their contact state, lubrication condition, and vibration response directly affect operational stability and fault evolution. For deep-groove ball bearings widely used in motors, pumps, machine tools, and automated production lines, localized defects such as raceway spalls, pitting, and local wear alter the load-transfer path between rolling elements and raceways and generate distinct impact features in the time-domain response. Accurate spall-size quantification therefore depends not only on signal-processing results, but also on the capability of dynamic models to describe contact force, stiffness/damping variation, and defect-induced excitation. Introducing lubricant-film behavior and thermal effects into localized-defect modeling is important for improving the reliability of spall-size estimation.

The rolling element–raceway contact is commonly simplified as Hertzian contact. Under lubricated operating conditions, however, oil-film pressure, film thickness, and temperature affect the load-carrying capacity, energy dissipation, and dynamic transmission characteristics of the contact interface. Zhang et al. [1] considered temperature effects in rolling-bearing dynamics, but did not explicitly introduce lubricant-film states into the contact parameters. The coupling between lubricated contact and bearing dynamics has been studied in tribodynamics: Rahnejat and Gohar [2] represented lubricated radial ball bearings by nonlinear spring–damper elements in rotor–bearing vibration analysis; Wijnant et al. [3] examined lubrication effects on ball-bearing dynamics; Sarangi et al. [4] formulated stiffness and damping coefficients for mixed-lubricated ball bearings; Mohammadpour et al. [5] developed a transient thermal-mixed non-Newtonian EHL framework linking contact load, lubrication state, and vibration response; and Zhang et al. [6] studied the dynamic behavior of elastohydrodynamically lubricated rolling contacts. These studies provide the basis for incorporating EHL/TEHL contact behavior into bearing dynamic analysis.

For bearings with localized defects, dynamic models have evolved from ideal Hertzian formulations to models considering defect geometry, time-varying displacement excitation, oil-film stiffness, skidding, and lubrication thermal effects. Luo et al. [7] described the displacement and excitation force caused by rolling elements passing through an inner-race spall using piecewise functions. Gomez et al. [8] modeled localized defects based on instantaneous angular speed variations, while Jiang et al. [9] improved defective-bearing modeling by considering the three-dimensional rolling element–defect geometry. Yan et al. [10] established a 5-DOF model under isothermal EHL conditions and analyzed lubrication-dependent stiffness and vibration response. Tian et al. [11] coupled bearing dynamics with TEHL to study contact force, friction force, and oil-film temperature in high-speed angular contact ball bearings. Wang et al. [12] showed that thermal EHL changes oil-film pressure, film thickness, and vibration amplitude in defective bearings. Tian et al. [13] further introduced rolling element spin, revolution, skidding, and TEHL effects into defective deep-groove ball bearing dynamics. Huo et al. [14] investigated locally failed roller bearings under starved lubrication. Bai et al. [15] studied lubrication state transitions in thermally affected defective bearings. Huo et al. [16] analyzed outer-ring localized failure under starved lubrication, and Peng et al. [17] considered rolling element–defect boundary interaction within a point-contact mixed-lubrication framework. These studies have advanced lubricated dynamic modeling of defective bearings, but most focus on global vibration response, contact load, skidding behavior, lubrication state variation, or defect-boundary interaction. The relationship between TEHL contact parameters and double-impact time characteristics for outer-ring spall-size quantification remains insufficiently clarified.

Double-impact features provide a direct physical basis for spall-size quantification. When a rolling element enters and exits a spalled region, two impact events with different physical meanings may appear in the vibration response, and their time interval is closely related to the spall length. Epps [18] first indicated that this interval increases with defect size. Randall and Sawalhi [19] developed signal-processing tools for spall tracking, and Sawalhi and Randall [20] verified the difference between entry and exit responses. Ming et al. [21] established a dual-impulse model based on acoustic emission signals. Singh and Kumar [22] and Jena and Panigrahi [23] used wavelet decomposition and vibration analysis for defect-width measurement. More recently, He et al. [24], Wu et al. [25], and Luo et al. [26] advanced spall-size evaluation through cross-condition diagnosis, dual-impulse behavior analysis, physical modeling, and instantaneous vibration energy. These studies confirm that the double-impact interval is an important indicator for spall-size estimation.

Although EHL/TEHL bearing dynamics and double-impact-based defect quantification have both been widely investigated, they have mainly developed along different modeling routes. Existing EHL/TEHL dynamic studies clarify how lubrication affects contact load, stiffness/damping, skidding, and vibration response, whereas double-impact-based quantitative diagnosis usually estimates defect size from impact timing, defect geometry, or vibration features. For outer-ring spalls, the remaining issue is not whether lubrication affects bearing dynamics, but how the local TEHL state is transferred into the dynamic quantities that determine the double-impact interval. In particular, the influence of oil-film pressure, film thickness, temperature field, and inner–outer raceway thermal asymmetry on equivalent stiffness/damping, oil-film-related displacement excitation, rolling element–raceway contact force, and spall-size estimation has not been sufficiently described.

To address this issue, this study focuses on the outer-ring spall defect of an SKF 6205 deep-groove ball bearing and adopts a 5-DOF bearing dynamic framework with contact-interface parameters reformulated under point-contact TEHL conditions. The TEHL-derived oil-film pressure, film thickness, temperature field, and inner–outer raceway thermal asymmetry are converted into an equivalent stiffness–damping representation. These contact parameters are then introduced into the dynamic framework together with oil-film-thickness-related additional-displacement excitation and rolling element–raceway contact force, thereby establishing the relationship between local lubricated contact behavior and the macroscopic double-impact response. Finally, the outer-ring spall size is estimated using the double-impact time interval and validated through numerical simulations and experiments.

2. Point-Contact Thermo-Elastohydrodynamic Lubrication Theory and Bearing Characteristic Modeling

To overcome the limitation of neglecting temperature-dependent lubricant-film effects in conventional models, a point-contact TEHL-based framework is developed, enabling accurate characterization of oil-film pressure, thickness, and temperature coupling, and facilitating an improved stiffness–damping model for enhanced dynamic analysis.

2.1. Limitations of Traditional Bearing Stiffness and Damping Models

Temperature fluctuations during prolonged operation alter rolling-bearing material properties, disrupting their dynamic models and lubrication performance. Excessive temperature aggravates lubrication deficiency and localized overheating, making investigation of temperature-dependent elastohydrodynamic lubrication behavior of bearing lubricants critical. This study focuses on the 6205 deep-groove ball bearing, whose parameters listed in Table 1.

Table 1. Geometric parameters of the 6205 deep-groove ball bearing.

Parameter Name	Value
Number of rolling elements N_b	9
Diameter of rolling element $D_b/(\mathrm{mm})$	7.938
Pitch circle diameter $D_p/(\mathrm{mm})$	38.5
Inner raceway diameter $D_i/(\mathrm{mm})$	30.562
Outer raceway diameter $D_o/(\mathrm{mm})$	46.438
Radial internal clearance $c/(\mu\mathrm{m})$	3
Contact angle $\alpha/(^\circ)$	0

https://doi.org/10.3390/lubricants14070261

Figure 1 presents two simplified rolling-bearing stiffness–damping models under TEHL conditions. Both models (Figure 1a,b) neglect oil-film thermal effect under temperature variation, which causes misjudgment of bearing capacity and oil-film stiffness, deviation of dynamic simulation from actual working conditions, and significant bias in quantitative spall-size calculation. TEHL theory is thus introduced to correct this oversight, enabling more accurate quantitative fault diagnosis of rolling bearings via realistic characterization of oil-film properties and their influence on macroscopic bearing parameters.

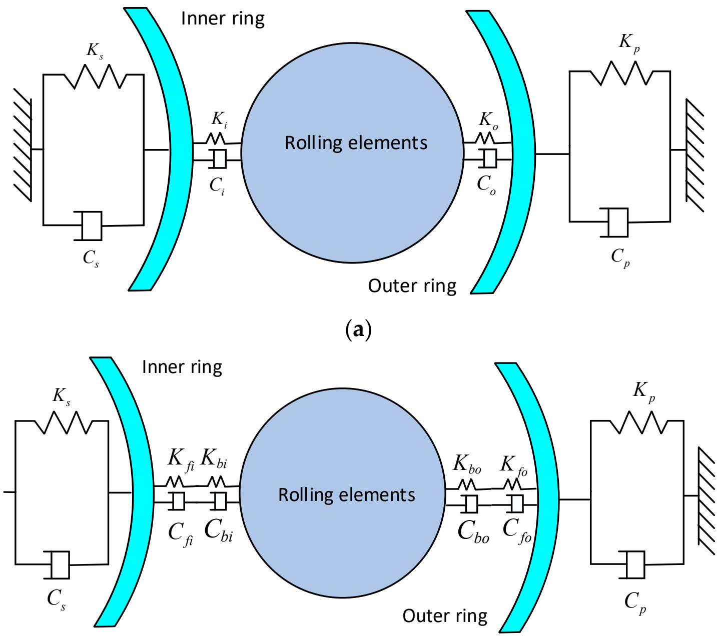

(**a**)

(**b**)

Figure 1. Summary of stiffness and damping characteristics of SKF 6205 bearing under different modeling conditions: (**a**) Simplified stiffness–damping model without bearing inner- and outer-ring oil-film stiffness and structural damping under TEHL conditions; (**b**) Simplified stiffness–damping model with bearing inner- and outer-ring oil-film stiffness and structural.

2.2. Numerical Simulation Modeling of Point-Contact Thermo-Elastohydrodynamic Lubrication

2.2.1. Numerical Simulation Model Construction

To characterize the temperature-dependent lubricant-film behavior of the rolling element–raceway contact, a point-contact TEHL model is first established. The calculated oil-film pressure, film thickness, and temperature fields provide the local contact-state variables required for the subsequent stiffness–damping representation and dynamic formulation.

For the ball–inner/outer raceway point-contact conjunctions of the 6205 bearing, the TEHL numerical model is solved using a multigrid method by coupling the Reynolds equation, the viscosity–pressure–temperature relation, the density relation, the elastic deformation equation, and the energy equation. No. 4106 aviation lubricant is selected as the lubricating medium, and its parameters are listed in Table 2.

The point-contact TEHL model is used to obtain the lubricant-film pressure, film thickness, temperature field, and the corresponding oil-film stiffness/damping of the ball–raceway contact, which are subsequently introduced into the bearing dynamic model. Therefore, the local lubrication problem is treated as a quasi-steady point-contact TEHL problem, while the time-varying response caused by the outer-ring spall is described in the dynamic model.

Table 2. Parameters of No. 4106 aviation lubricating oil.

Parameter Name and Unit	Value
Thermal Conductivity $k_h/(\mathrm{W}/(\mathrm{m}\cdot\mathrm{K}))$	0.0966
Viscosity–Pressure Coefficient $\alpha/(\mathrm{Pa}^{-1})$	1.85×10^{-8}
Viscosity–Temperature Coefficient $\beta/(\mathrm{K}^{-1})$	0.0315
Specific Heat Capacity $c_h/(\mathrm{J}/(\mathrm{kg}\cdot\mathrm{K}))$	2000
Ambient Temperature $T_0/(\mathrm{K})$	298.15
Initial Viscosity $\eta_0/(\mathrm{Pa}\cdot\mathrm{s})$	0.055
Initial Density $\rho_0/(\mathrm{kg}/\mathrm{m}^3)$	890

(1) Reynolds equation

For the SKF 6205 bearing, the ball–raceway contact is modeled as a fully flooded elliptical point contact. The x- and y-directions are defined along the rolling direction and the transverse direction of the contact ellipse, respectively. Surface motion is assumed to be dominated by rolling entrainment in the x-direction, with the entrainment velocity defined as u_e = (u1 + u2)/2. The y-direction pressure-flow term is retained to describe transverse pressure diffusion, whereas lateral entrainment and the transient squeeze-film term 12∂(ρh)/∂t are not included in the local Reynolds equation. Under these assumptions, the Reynolds equation used in the point-contact TEHL calculation is written as

$$\left(\frac{\partial}{\partial x}\right)\left(\left(\frac{\rho h^3}{\eta}\right)\left(\frac{\partial p}{\partial x}\right)\right)+\left(\frac{\partial}{\partial y}\right)\left(\left(\frac{\rho h^3}{\eta}\right)\left(\frac{\partial p}{\partial y}\right)\right)=12u_e\left(\frac{\partial(\rho h)}{\partial x}\right) \tag{1}$$

where h is the oil-film thickness, p is the oil-film pressure, η is the lubricant viscosity, ρ is the lubricant density, and u_e is the entrainment velocity in the rolling direction. In a fully transient TEHL formulation, the squeeze-film contribution is associated with the instantaneous normal approach or separation of the contacting surfaces. In this study, this impact-induced approach and separation are represented at the bearing-system level through the time-varying contact deformation, additional-displacement excitation, rolling element–raceway contact force, and TEHL-derived equivalent stiffness/damping, as described in Section 3.

(2) Viscosity variation equation (dependent on pressure and temperature):

For the selected 4106 aviation lubricant, the viscosity in the point-contact TEHL calculation is evaluated as a function of the local pressure and temperature. The Roelands viscosity relation, expressed using Houpert's pressure–viscosity and temperature–viscosity indices, is adopted as follows [27,28]:

$$\eta=\eta_0\exp\left((\ln\eta_0+9.67)\times\left[-1+\left(1+5.1\times10^{-9}p\right)^{(z_0)}\left(\frac{T-138}{T_0-138}\right)^{-s_0}\right]\right) \tag{2}$$

$$z_0=\frac{\alpha}{5.1\times10^{-9}(\ln\eta_0+9.67)} \tag{3}$$

$$s_0=\frac{\beta(T_0-138)}{\ln\eta_0+9.67} \tag{4}$$

where T_0 is the ambient temperature, T is the oil-film temperature, η_0 is the initial viscosity of the lubricant, α is the viscous pressure coefficient, β is the viscous temperature coefficient, and z_0 and s_0 are the pressure–viscosity index and temperature–viscosity index in the Roelands–Houpert formulation, respectively.

(3) The lubricant density is described using the Dowson–Higginson density–pressure relation with a temperature correction [29]:

$$\rho = \rho_0 \left[1 + \frac{0.6 \times 10^{-9} p}{1 + 1.7 \times 10^{-9} p} - 6.5 \times 10^{(-4)(T - T_0)} \right] \tag{5}$$

where ρ_0 is the initial density of the lubricant.

(4) Point-contact elastic deformation equation

The solution domain for the point-contact deformation is a rectangular region, as shown in Figure 2a. In the solution domain, AB is defined as the entrance edge, CD as the exit edge, and AD and BC as the end drain edges.

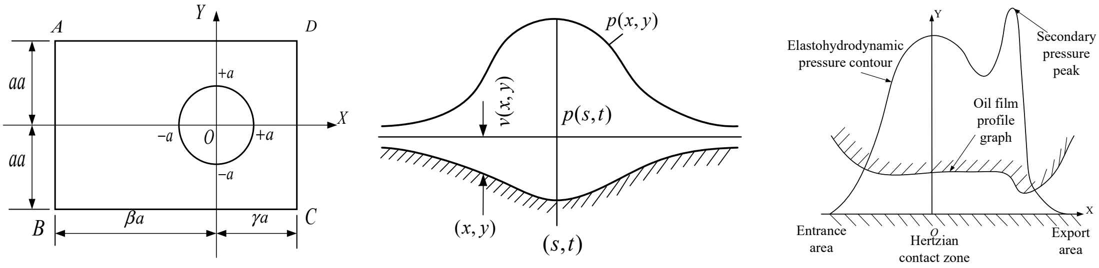

(**a**) (**b**) (**c**)

Figure 2. Schematic diagrams for the point-contact TEHL model: (**a**) point-contact solution domain; (**b**) equivalent elastic deformation model; (**c**) theoretical distribution of oil-film shape and elastohydrodynamic pressure.

Following the point-contact EHL formulation, the two elastic bodies are reduced to an equivalent elastic body and a rigid plane, as shown in Figure 2b. The local film thickness $h(x, y)$, consisting of the central film thickness, geometric separation, and pressure-induced elastic deformation $v(x, y)$, is expressed as [30]:

$$h(x, y) = h_0 + \frac{x^2}{2R_x} + \frac{y^2}{2R_y} + v(x, y) \tag{6}$$

$$v(x, y) = \frac{2}{\pi E'} \iint_{\Omega} \frac{p(s, t)}{\sqrt{(x - s)^2 + (y - t)^2}} dsdt \tag{7}$$

where h_0 is the undeformed central film thickness, R_x and R_y are the equivalent curvature radii, E' is the equivalent elastic modulus, $p(s, t)$ is the contact pressure, s and t are integration coordinates, and Ω is the solution domain.

The theoretical oil-film shape and elastohydrodynamic pressure distribution are shown in Figure 2c. The pressure distribution exhibits a typical secondary pressure peak near the outlet region.

(5) The oil-film temperature field is obtained from the thermal EHL energy equation [31]:

$$c_o \left(\rho u \frac{\partial T}{\partial x} + \rho v \frac{\partial T}{\partial y} - q \frac{\partial T}{\partial z} \right) = \frac{k_o \left(\partial^2 T \right)}{\partial z^2} - \left(\frac{\partial \rho}{\partial T} \right) \left(\left(\frac{uT}{\rho} \right) \left(\frac{\partial p}{\partial x} \right) + \left(\frac{vT}{\rho} \right) \left(\frac{\partial p}{\partial y} \right) \right) + \eta \left[\left(\frac{\partial u}{\partial z} \right)^2 + \left(\frac{\partial v}{\partial z} \right)^2 \right] \tag{8}$$

where k_o represents the thermal conductivity of the lubricant, and c_o denotes the specific heat capacity of the lubricant.

(6) The heat transfer at the rolling element–lubricant and raceway–lubricant interfaces is described using thermal boundary conditions derived from moving heat-source theory [32]:

$$\begin{cases} T(x,y,0) = \frac{k_h}{\sqrt{\pi \rho_1 c_1 k_1 u_1}} \int_{-\infty}^{x} \left(\frac{\partial T}{\partial z|_{x,y,0}} \right) d \frac{s}{\sqrt{x-s}} + T_0 \\ (x,y,h) = \frac{k_h}{\sqrt{\pi \rho_2 c_2 k_2 u_2}} \int_{-\infty}^{x} \left(\frac{\partial T}{\partial z|_{x,y,h}} \right) d \frac{s}{\sqrt{x-s}} + T_0 \end{cases} \tag{9}$$

where ρ, c, k denote the density, specific heat capacity and heat transfer coefficient of the contact pair; subscripts 1 and 2 refer to the rolling element and raceway, respectively.

2.2.2. Analysis of Numerical Simulation Results

Via the aforementioned coupled equations and multigrid method, the pressure distribution, film thickness distribution and oil-film temperature map under the point-contact TEHL state are derived, as depicted in Figure 3a–c, respectively.

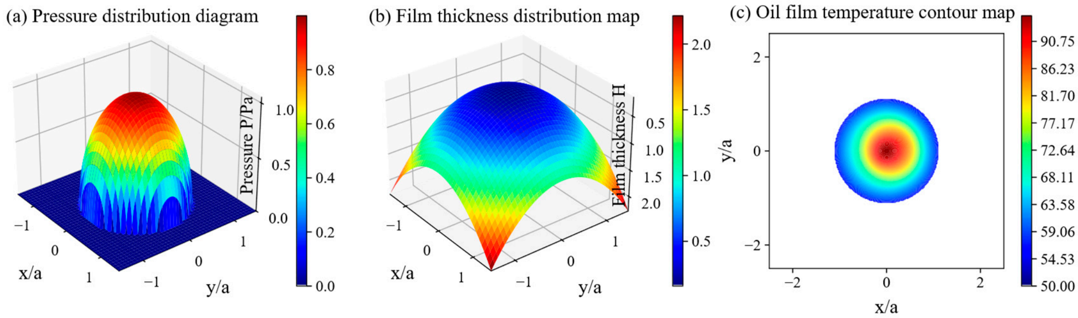

Figure 3. Numerical results of the point-contact TEHL model.

As shown in Figure 3a–c, the point-contact TEHL model presents typical elastohydrodynamic lubrication characteristics. The pressure distribution exhibits a secondary pressure peak near the outlet region, which is consistent with the theoretical distribution shown in Figure 2c and supports the validity of the model.

2.3. Improved Rolling-Bearing Stiffness and Damping Model Considering Thermo-Elastohydrodynamic Lubrication

2.3.1. Improved Bearing Stiffness and Damping Models

Under point-contact TEHL conditions, the rolling element is separated from the inner and outer raceways by lubricant films, forming an inner raceway–oil film–rolling element–oil film–outer raceway contact system. The solid-contact component of this system is described by the Hertzian load–deformation relation [33]. For the ball–raceway contact considered in this study, the nonlinear normal contact force is expressed as:

$$F = K\,\delta^n \tag{10}$$

where F denotes the nonlinear contact force, δ is the contact deformation displacement, K is the contact stiffness coefficient, and n is the load–deflection index, which is usually taken as $n = 1.5$ for ball bearings.

Under TEHL conditions, the rolling element–raceway contact is represented by the simplified stiffness–damping form shown in Figure 4.

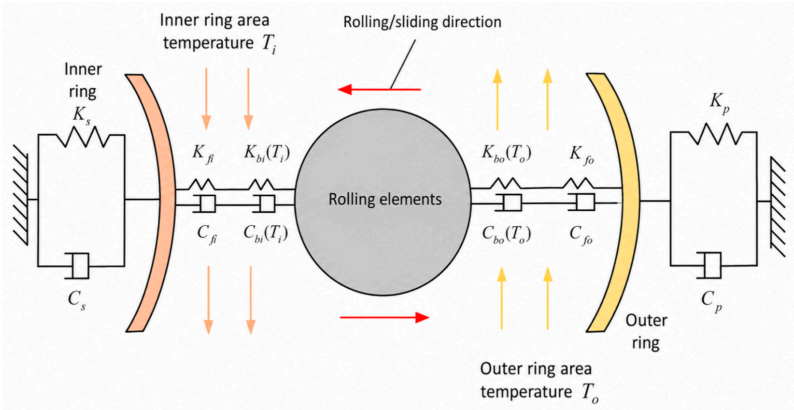

Figure 4. Simplified stiffness–damping representation of the rolling element–raceway contact under TEHL conditions.

Figure 4 shows the stiffness–damping representation of the bearing contact interface under TEHL conditions. In this representation, the rolling element–raceway contact is not described only by a prescribed Hertzian contact parameter. Instead, the inner- and outer-raceway contact characteristics are represented by the combined effects of Hertzian contact stiffness/damping and TEHL-derived oil-film stiffness/damping. Different temperature parameters are introduced for the inner and outer raceways to capture the thermal asymmetry of the lubricated contact. The minimum oil-film thickness and rotational speed are taken as the key variables for calculating the equivalent stiffness and damping. These equivalent parameters provide the contact-interface input for the subsequent 5-DOF dynamic formulation.

2.3.2. Rolling-Bearing Stiffness Calculation

The stiffness–damping representation of the bearing contact interface includes the Hertzian contact stiffness between the rolling elements and the inner/outer raceways and the lubricant-film stiffness. The Hertzian contact stiffness is calculated based on Hertzian contact theory and rolling-bearing contact analysis [33,34]:

$$\begin{cases} K_{bi} = \dfrac{2\sqrt{2\left(\frac{E}{1-\nu^2}\right)}}{3\left(\sum\rho_i\right)^{\frac{1}{2}}}\left(\dfrac{1}{\delta_i}\right)^{\frac{3}{2}} \\ K_{bo} = \dfrac{2\sqrt{2\left(\frac{E}{1-\nu^2}\right)}}{3\left(\sum\rho_o\right)^{\frac{1}{2}}}\left(\dfrac{1}{\delta_o}\right)^{\frac{3}{2}} \end{cases} \tag{11}$$

where K_{bi}, K_{bo} represent the initial contact stiffnesses between rolling elements and the inner/outer raceways, respectively; $\sum\rho_i$, $\sum\rho_o$ represent the curvatures of the inner/outer raceways; δ_i, δ_o represent the contact displacements of unit magnitude for the inner/outer raceways; E represents the elastic modulus; and ν represents the Poisson's ratio.

Under TEHL conditions, oil-film stiffness is defined as the ratio of the radial load to the radial deformation of the oil film. For the calculation of oil-film stiffness, the oil-film stiffness of the bearing's inner/outer rings can be derived as follows:

$$K_{fi} = K_{fo} = \frac{\lim_{\delta\to 0}\Delta\omega}{\delta} = -\frac{d\omega}{dh} = \lim_{\Delta\to 0}\frac{\Delta Q_{\max}}{\Delta h_{mt}} = \frac{\partial\left(\iint_\Omega p(x,y)dx\,dy\right)}{\partial h_{mt}} \tag{12}$$

where h_{mt} denotes the minimum oil-film thickness under TEHL conditions.

The equivalent stiffness of the inner ring, K_s, the equivalent stiffness of the outer ring, K_p, and the integrated stiffness of the bearing, K_b, are calculated as follows:

$$K_s = \frac{K_{bi}(T_i)K_{fi}}{K_{bi} + K_{fi}} \tag{13}$$

$$K_p = \frac{K_{bo}(T_o)K_{fo}}{K_{bo}(T_o) + K_{fo}} \tag{14}$$

$$K_b = \frac{K_s K_p}{K_s + K_p} \tag{15}$$

2.3.3. Calculation of Rolling Bearing Damping

The calculation formula of the bearing's structural damping under TEHL conditions is given as follows [35]:

$$C_{bi} = C_{bo} = \frac{\eta_b \cdot k_{i-o}}{\omega_{\text{ext}}} \tag{16}$$

where η_b is the bearing structural loss factor, and ω_{ext} is the excitation frequency. Under thermo-elastohydrodynamic lubrication, C_{bi} represents the structural damping of the inner ring of the bearing and C_{bo} represents the structural damping of the outer ring of the bearing as the initial structural damping, k_{i-o} denotes the equivalent stiffness between the inner and outer rings of a rolling bearing.

Under TEHL conditions, oil-film damping is defined as the ratio of the variation in load acting on the oil film to the variation in contact velocity. The oil-film damping of the bearing's inner and outer rings is given as follows:

$$C_{fi} = C_{fo} = \lim\nolimits_{\Delta \to 0} \frac{\Delta Q_{\max}}{\Delta u_s} = \frac{\partial\left(\iint_\Omega p(x,y)dx\,dy\right)}{\partial u_s} \tag{17}$$

where C_{fi} and C_{fo} denote the TEHL-derived oil-film damping components of the rolling element–inner raceway contact and rolling element–outer raceway contact, respectively; $\Delta Q_{\max}$ denotes the variation in the maximum oil-film load; Δu_s is the variation in relative sliding/contact velocity; $p(x,y)$ denotes the pressure distribution in the contact area; and Ω is the integral domain of the contact area.

The equivalent damping C_s of the inner ring, the equivalent damping C_p of the outer ring, and the integrated damping C_b of the bearing are calculated as follows:

$$C_s = \frac{C_i(T_i)C_{fi}}{C_i(T_i) + C_{fi}} \tag{18}$$

where $C_i(T_i)$ represents the temperature-dependent structural/contact damping component of the inner-raceway side at temperature T_i, C_{fi} represents the TEHL-derived oil-film damping between the rolling element and the inner raceway, and C_s is the equivalent damping of the inner-raceway side.

$$C_p = \frac{C_o(T_o)C_{fo}}{C_o(T_o) + C_{fo}} \tag{19}$$

where $C_o(T_o)$ represents the temperature-dependent structural/contact damping component of the outer-raceway side at temperature T_o, C_{fo} represents the TEHL-derived oil-film damping between the rolling element and the outer raceway, and C_p is the equivalent damping of the outer-raceway side.

$$C_b = \frac{C_s C_p}{C_s + C_p} \tag{20}$$

where C_b is the total damping of the rolling bearing.

Based on Equations (11)–(20), the equivalent stiffness and damping of the inner- and outer-raceway contacts are obtained under point-contact TEHL conditions. These parameters combine the Hertzian solid-contact component with the lubricant-film component and include the temperature difference between the inner and outer raceways. The obtained equivalent stiffness and damping are then used as contact-interface parameters in the subsequent dynamic formulation.

3. Modeling and Quantitative Diagnostic Study of Rolling-Bearing Dynamics Under TEHL

Based on the point-contact TEHL model and the stiffness–damping representation developed in Section 2, this section introduces the TEHL-derived contact-interface parameters into a 5-DOF bearing dynamic framework to analyze the double-impact response of rolling bearings with outer-ring spall defects. The oil-film thickness, equivalent stiffness/damping, and contact force are then used to establish the relationship between the lubricated contact state and spall-size quantification.

3.1. Excitation Model for Additional Displacement of Rolling Element–Raceway Contact Under TEHL

Under TEHL conditions, lubricant films exist between the rolling element and the inner/outer raceways, so the rolling element–raceway contact displacement differs from that under dry-contact conditions. The lubricant film modifies the local contact clearance, load transfer, and energy dissipation, thereby affecting the double-impact response induced by outer-ring spalls. Therefore, the oil-film thickness is introduced into the additional-displacement excitation model to describe the variation in rolling element–raceway separation when the rolling element passes through the outer-ring spall.

The oil-film thickness used in the additional-displacement model is calculated using the Hamrock and Dowson film-thickness relation for fully flooded elliptical elastohydrodynamic contacts, with the oil-film thickness correction factor f_T introduced for the TEHL condition [36]:

$$h_{i/o} = 3.63\, V^{0.68}\, M^{0.49}\, W^{-0.073}\left(1 - 0.61e^{-0.73\kappa}\right) R_x\, f_T \tag{21}$$

where V denotes the dimensionless speed parameter; M denotes the dimensionless material parameter; W denotes the dimensionless load parameter; R_x denotes the equivalent radius of curvature of the two contacting bodies along the rolling direction of the bearing; and κ denotes the contact ellipse parameter. h_i represents the central oil-film thickness between the inner ring and the rolling element, and h_o represents the central oil-film thickness between the outer ring and the rolling element. f_T denotes the oil-film thickness correction factor. Based on Equation (21), the radial contact deformation between the rolling element and the inner/outer rings under point-contact TEHL conditions is compared for the fault-free and faulty states.

The Hertzian contact deformation of the rolling elements under TEHL conditions is shown in Figure 5a, and the radial displacement geometry is presented in Figure 5b, where the orange area represents the oil film.

Based on the geometric relationship shown in Figure 5b, the radial deformation of the first rolling element and the inner/outer rings under fault-free operation can be written as:

$$\delta_{j1} = (x_s - x_p)cos\phi_j + (y_s - y_p)sin\phi_j - c - h_i - h_o \tag{22}$$

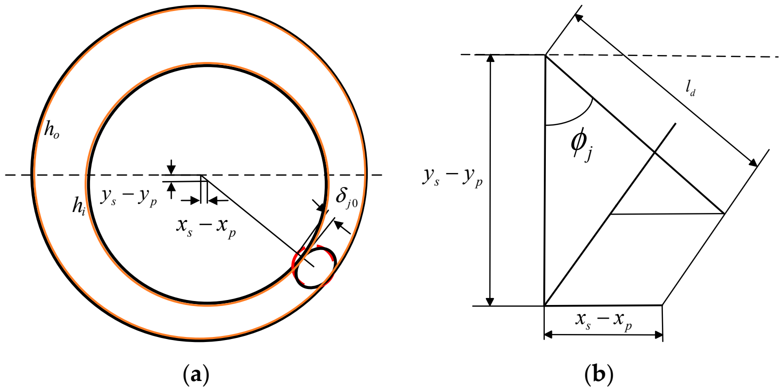

Figure 5. Contact deformation and radial displacement relationship of the rolling element–raceway contact under TEHL conditions: (**a**) Hertzian contact deformation of the rolling element; (**b**) geometric relationship of radial displacement, where the orange region denotes the lubricating oil film.

Secondly, when the outer ring fails, the radial deformation between the first rolling element and the inner and outer rings is converted to the total contact displacement model under point-contact thermo-elastohydrodynamic lubrication:

$$\delta_{j0} = (x_s - x_p)cos\phi_j + (y_s - y_p)sin\phi_j - c - h_i - h_o - \beta_j l_d \tag{23}$$

where l_d is the additional displacement.

To determine whether the bearing is in the fault zone, the same switching function β_j is introduced as follows:

$$\begin{cases} 1 & \phi_d < \phi_j < \phi_d + \Delta\phi_d \\ 0 & otherwise \end{cases} \tag{24}$$

where ϕ_d and $\Delta\phi_d$ denote the initial angular position and the angular width of the spalled area, respectively. For rolling bearings with outer-ring spalls, assuming the outer ring is fixed and the inner ring rotates, the theoretical time required for a rolling element to traverse this defect zone is denoted by T_{spall}. Based on the geometric relationship, the quantitative mapping between this double-impact time interval and the outer-ring spall size L_{spall} can be explicitly expressed as $L_{\text{spall}} = 2r_0 sin(\omega_c T_{\text{spall}}/2)$, where r_0 is the corresponding radius of the raceway.

3.2. Calculation of Rolling Element–Raceway Contact Force Under TEHL

Under the action of an external radial load, the inner and outer rings undergo radial displacement, inducing contact deformation and corresponding nonlinear contact forces. To calculate these forces under TEHL conditions, the bearing kinematics must first be defined. The angular velocity of the cage (and the rolling elements) is given by $\omega_c = (1 - D_b/D_p)\omega_s/2$, where D_b and D_p are the rolling element and pitch circle diameters, respectively, and ω_s is the shaft angular velocity. Consequently, the instantaneous angular position of the $j - th$ rolling element is $\phi_j = 2\pi(j-1)/n_b + \omega_c dt + \phi_0$, where n_b is the total number of rolling elements, and ϕ_0 is the initial phase.

To integrate the complex TEHL characteristics into the classical dynamic framework efficiently, a quasi-static nonlinear approximation is widely adopted in engineering modeling. Specifically, the improved equivalent stiffness K_b is substituted into the classical 3/2 power law to approximate the macroscopic nonlinear contact force F_j:

$$F_j = K_b \delta_j^{1.5} \tag{25}$$

where K_b is the combined stiffness of the improved bearing stiffness and damping model under TEHL, and δ_j is the contact deformation of the j-th rolling element.

The nonlinear contact forces of the rolling bearing in the X and Y directions are, respectively:

$$f_x = K_{b\sum\gamma_j}\,\delta_j^{\frac{3}{2}}\ \cos(\phi_j) = \frac{K_s K_p}{K_s + K_p}\sum\gamma_j\delta_j^{\frac{3}{2}}\ \cos(\phi_j) \tag{26}$$

$$f_y = K_{b\sum\gamma_j}\,\delta_j^{\frac{3}{2}}\ \sin(\phi_j) = \frac{K_s K_p}{K_s + K_p}\sum\gamma_j\delta_j^{\frac{3}{2}}\sin(\phi_j) \tag{27}$$

The rolling element contributes to the contact force only when it is in the loaded contact region. Therefore, the following switching function is introduced:

$$\gamma_j = \begin{cases} 1 & \delta_j > 0 \\ 0 & otherwise \end{cases} \tag{28}$$

The Hertzian contact force f_x in the horizontal direction of a rolling bearing, for example, varies as follows:

$$f_x = \begin{cases} \frac{K_s K_p}{K_s+K_p}\sum\gamma_j\delta_j^{\frac{3}{2}}\cos(\phi_j) & \text{non} - \text{faulty area} \\ 0\ \ otherwise & \text{faulty area} \end{cases} \tag{29}$$

The Hertzian contact force f_y in the vertical direction of a rolling bearing, for example, varies as follows:

$$f_y = \begin{cases} \frac{K_s K_p}{K_s+K_p}\sum\gamma_j\delta_j^{\frac{3}{2}}\sin(\phi_j) & \text{non} - \text{faulty area} \\ 0\ \ otherwise & \text{faulty area} \end{cases} \tag{30}$$

Equations (29) and (30) describe the horizontal and vertical components of the rolling element–raceway contact force, respectively. Since the subsequent vibration analysis focuses on the vertical response, the vertical contact-force component f_y is used in the following discussion.

3.3. Equation Construction of Rolling-Bearing Dynamics Under TEHL

The 5-DOF dynamic equations used in this section follow the classical bearing/spindle vibration framework reported by Aini et al. [37]. In this framework, the stiffness and damping coefficients associated with the rolling element–raceway contacts are generally treated as prescribed bearing parameters. In the present formulation, the equation structure is retained, while the contact-related terms are parameterized using the equivalent stiffness and damping obtained in Section 2.3. Specifically, the equivalent stiffness and damping include the Hertzian contact stiffness/damping, TEHL-derived oil-film stiffness/damping, and the thermal asymmetry between the inner and outer raceways.

Based on the additional-displacement excitation model and the rolling element–raceway contact-force model under TEHL conditions, these equivalent contact parameters are introduced into the 5-DOF formulation for a rolling bearing with an outer-ring spall defect. Thus, the oil-film pressure, film thickness, and temperature field calculated at the contact interface are transmitted to the system-level dynamic response through the equivalent stiffness/damping, additional-displacement excitation, and nonlinear contact force. The parameters used for the 6205 deep-groove ball bearing are listed in Table 3.

The schematic diagram of the outer-ring spalling defect under TEHL conditions is shown in Figure 6. The dynamic equation for the outer-ring spalling defect of rolling bearings under TEHL is given in Equation (31).

$$\begin{cases} m_s\ddot{x}_s + C_s\dot{x}_s + K_s x_s + f_x = 0 \\ m_s\ddot{y}_s + C_s\dot{y}_s + K_s y_s + f_y = F_r \\ m_p\ddot{x}_p + C_p\dot{x}_p + K_p x_p - f_x = 0 \\ m_p\ddot{y}_p + (C_p + c_r)\dot{y}_p + (K_p + k_r)y_p - k_r y_b - c_r\dot{y}_b - f_y = 0 \\ m_r\ddot{y}_b + c_r(\dot{y}_b - \dot{y}_p) + k_r(y_b - y_p) = 0 \end{cases} \tag{31}$$

Table 3. Parameters used in the TEHL-based 5-DOF dynamic model of the 6205 deep-groove ball bearing.

Parameter Name	Value and Unit	Parameter Name	Value and Unit
Inner race and shaft mass m_s	1.2638 kg	Unit resonator mass m_r	1 kg
Outer race and shaft stiffness K_s	4.241×10^4 N/m	Unit resonator stiffness k_r	8.8826×10^9 N/m
Inner race and shaft damping C_s	2376.8 N s/m	Unit resonator damping c_r	9424.8 N s/m
Outer race and base mass m_p	12.638 kg	Outer race and base stiffness K_p	15.1056×10^6 N/m
Outer race and base damping C_p	2210.7 N s/m	Contact stiffness K_d	1.8918×10^{10} N/m

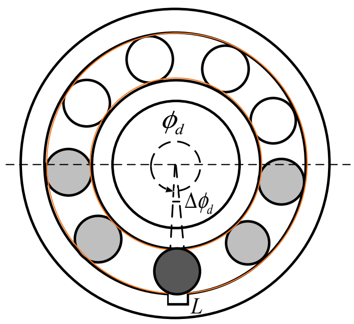

Figure 6. Schematic diagram of an outer-ring failure in a rolling element.

Equation (31) represents the 5-DOF dynamic formulation used for the outer-ring spall bearing under TEHL conditions. The equation structure follows the classical 5-DOF framework, while the stiffness, damping, and contact-force terms are supplied by the TEHL-based stiffness–damping representation. The formulation includes the motion of the inner race and shaft, the outer race and base, and the unit resonator coupled to the outer-race/base system in the y direction. In this equation, m_s is the mass of the inner race and shaft, m_p is the mass of the outer race and base, and m_r is the mass of the unit resonator. K_s and C_s are the equivalent stiffness and damping of the inner-race side obtained from the stiffness–damping representation under TEHL conditions, while K_p and C_p are the corresponding equivalent stiffness and damping of the outer-race side. The parameters k_r and c_r denote the stiffness and damping of the unit resonator, respectively, and they describe the coupling between the unit resonator displacement y_b and the outer-race/base displacement y_p. The terms f_x and f_y are the nonlinear rolling element–raceway contact force components in the x and y directions, respectively, and F_r is the radial load applied to the inner race in the y direction. The displacement variables x_s and y_s denote the motion of the inner race and shaft in the x and y directions, respectively; x_p and y_p denote the motion of the outer race and base in the x and y directions, respectively; and y_b denotes the displacement of the unit resonator in the y direction. The overdot and double overdot denote velocity and acceleration, respectively.

3.4. Simulation and Mechanism Analysis of Rolling-Bearing Impact Characteristics Under TEHL

3.4.1. Vibration Response and Contact Force Analysis for Two Defect Sizes

The TEHL-parameterized dynamic formulation is applied to a 6205 deep-groove ball bearing. The simulation conditions are as follows: a sampling frequency of 1.2 kHz, a rotational speed of 1000 rpm, a radial load of 500 N, two representative outer-ring defect widths of 4.2 and 0.5 mm, and a constant defect depth of 1.25 mm. Numerical integration is performed using the fourth-order Runge–Kutta method, and the vibration signals together with the vertical Hertzian contact forces are extracted over 0.224–0.2315 s for comparison. Figure 7a,b show the simulated responses for the large and small defects, respectively. As the defect size decreases, the rolling element enters the defective zone later, consistent with the actual fault evolution characteristics.

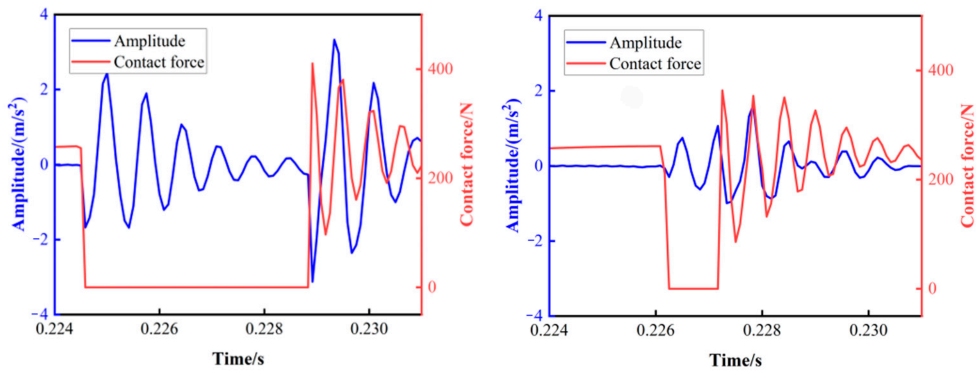

(**a**) 4.2 mm (**b**) 0.5 mm

Figure 7. Simulated signals versus Hertzian contact force variation for rolling-bearing defects of different sizes.

3.4.2. Comparison and Mechanism Exploration of Impact Phenomena Associated with Large-Size and Small-Size Failures

To compare the impact responses predicted by the TEHL-parameterized formulation for different defect sizes, an outer-ring spall with a size of 4.2 mm is defined as a large defect, whereas a 0.5 mm spall is defined as a small defect. The local impact components are magnified in Figure 8, where characteristic points A, B, C, D, A1, B1, C1, and D1 are marked for comparison.

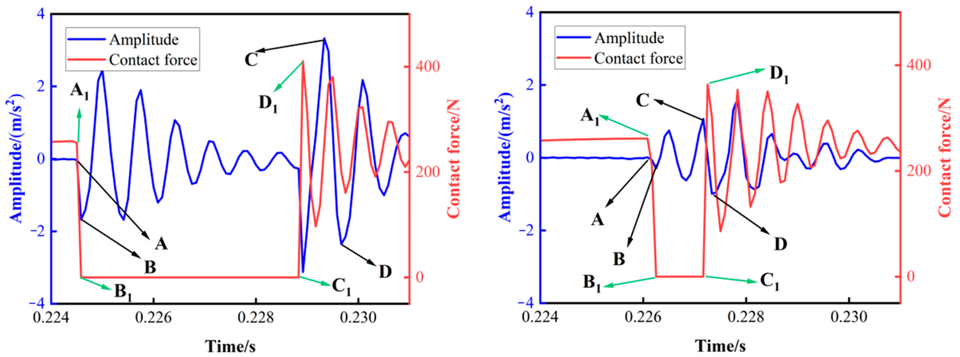

(**a**) 4.2 mm outer-ring failure (**b**) 0.5 mm outer-ring failure

Figure 8. Localized enlargement of rolling-bearing outer-ring fault signals.

A comparison of Figure 8a,b shows that the 4.2 mm outer-ring spall exhibits a clear double-impact characteristic, whereas the 0.5 mm spall presents only a weak double-impact or single-impact feature. In both cases, points A/A1 correspond to the instant when the rolling element enters the defective zone and triggers the entry impact, while points B/B1 indicate the rapid decay of the contact force to a minimum or zero within the fault region. Points C/C1 denote the instant when the rolling element leaves the defective zone and generates the exit impact. Points D/D1 indicate the subsequent post-exit local response extrema after the rolling element leaves the defective zone. They are used as auxiliary markers to illustrate the post-impact vibration and contact-force evolution, whereas points A and C are used for the subsequent spall-size quantification. For the large defect, the time interval between the entry and exit impacts is sufficiently long, resulting in a distinct double-impact pattern. For the small defect, the two impacts tend to overlap, leading to a weakened double-impact or an apparent single-impact response. Therefore, points A and C are selected as the characteristic instants for subsequent spall-size quantification, and the corresponding contact-force evolution is consistent with the time-domain response predicted by Equation (31).

3.5. Quantitative Diagnosis of Localized Defects Based on the TEHL Model

3.5.1. Dynamic Model Validation and Characteristic Point Analysis at Different Rotational Speeds

For the quantitative diagnosis of local defects based on the TEHL-parameterized formulation, two rotational speeds (500 rpm, 1500 rpm) were set, along with a radial load of 500 N, an outer-ring spall size of 2 mm, and a sampling frequency of 1.2 kHz. Time-domain diagrams of the TEHL-parameterized formulation and enlarged views of the local feature-point markers are presented in Figures 9 and 10.

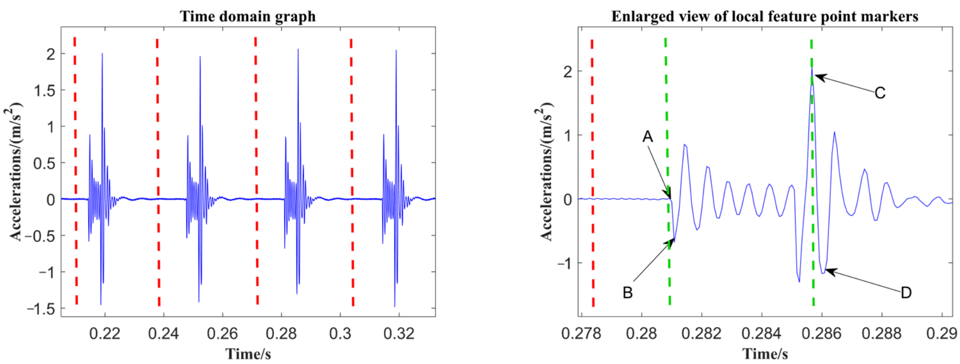

(**a**) Time-domain graph (**b**) Enlarged view of local feature-point markers

Figure 9. Time-domain response of a 2 mm outer-ring fault at 500 rpm, obtained from the TEHL-parameterized formulation with local feature-point markers.

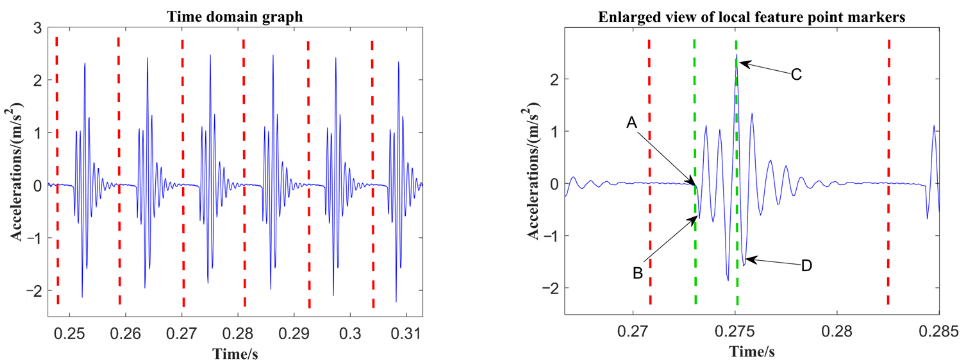

(**a**) Time-domain graph (**b**) Enlarged view of local feature-point markers

Figure 10. Simulated time-domain response plot at 1500 rpm for a 2 mm outer ring, with the local feature-point markers zoomed in.

As shown in Figures 9a and 10a, the simulated impact responses exhibit periodic features corresponding to repeated rolling-element passages over the outer-ring spall. This periodic behavior is consistent with the expected defect-passing mechanism and supports the dynamic consistency of the TEHL-parameterized formulation.

In Figures 9b and 10b, the local responses are enlarged to facilitate characteristic-point identification. Points A and C are identified as the entry-impact and exit-impact instants, denoted by (t_A) and (t_C), respectively. Points B and D denote the adjacent local response extrema following the entry and exit impacts, respectively. They are used as auxiliary markers to illustrate the local oscillatory response around the two impacts, whereas only points A and C are used to determine the double-impact interval ($t_C - t_A$) for the subsequent spall-size calculation. The green dotted lines mark the identified entry- and exit-impact instants, while the red dotted lines indicate the selected fault-passing period or localized time window. As the rotational speed increases, the interval ($t_C - t_A$) decreases, which is consistent with the shorter time required for the rolling element to pass through the spalled region. The outer-ring spall size is then calculated using the double-impact time-interval quantification formula derived from the TEHL-parameterized formulation:

$$L_{\text{spall}} = 2r_0 sin\left(\frac{\omega_c(t_C - t_A)}{2}\right) \tag{32}$$

where L_{spall} is the outer-ring spall length, r_0 denotes the radius corresponding to the outer-raceway spall trajectory, ω_c is the cage angular velocity, and t_A and t_C are the entry-impact and exit-impact instants identified from the double-impact response, respectively.

3.5.2. Comparative Analysis of Spall-Size Estimation Accuracy Using Different Dynamic Formulations

To verify the accuracy of the proposed quantitative rolling-bearing fault diagnosis method based on point-contact TEHL, the 5-DOF formulation with TEHL-based stiffness–damping parameters is compared with conventional 5-DOF, 4-DOF, and 2-DOF dynamic models. Quantitative calculations are performed for six spall sizes (0.2, 0.6, 1.2, 2.0, 3.0, and 4.2 mm) at a rotational speed of 1000 rpm. The corresponding error comparison results are presented in Table 4.

Table 4. Quantitative comparison of spall-size estimates obtained using different dynamic formulations.

Reference Spall Size (mm)	TEHL-Parameterized 5-DOF Formulation (mm)	Conventional 5-DOF Model (mm)	Conventional 4-DOF Model (mm)	Conventional 2-DOF Model (mm)
0.2	0.212	0.235	0.251	0.188
0.6	0.632	0.648	0.671	0.495
1.2	1.242	1.291	1.398	0.925
2.0	2.041	2.096	2.235	1.734
3.0	3.040	3.093	3.204	2.758
4.2	4.225	4.296	4.382	3.951

As shown in Table 4, the 5-DOF formulation with the TEHL-based stiffness–damping representation gives the closest estimates to the reference spall sizes among the compared models. For the six spall sizes of 0.2, 0.6, 1.2, 2.0, 3.0, and 4.2 mm, the relative errors are 6.00%, 5.33%, 3.50%, 2.05%, 1.33%, and 0.60%, respectively. This significant improvement in quantitative diagnostic accuracy is fundamentally attributed to the physical nature of the TEHL oil film. In conventional dry-contact models, the double-impact time interval is determined solely by the rigid defect geometry and solid kinematics. In contrast, the proposed model reveals that the oil film essentially acts as an additional dynamic clearance and a damping buffer. As the rolling element enters and exits the spall, the load-dependent variation in oil-film thickness alters the actual spatial trajectory of the rolling element. Concurrently, oil-film damping induces a subtle phase delay in the transient impact force peaks (e.g., characteristic points A and C). Consequently, incorporating these TEHL characteristics provides a more physically meaningful time-interval mapping for spall-size evaluation, thereby reducing the estimation deviation associated with purely elastic contact models.

4. Experimental Validation

4.1. Experimental Equipment and Bearing Failure Parts

To validate the accuracy of the proposed TEHL-based quantitative diagnosis method, artificial bearing faults were introduced using the HZXT-DS-003 (DongHua Testing Technology Co., Ltd., Jingjiang, China) double-span, double-rotor rolling-bearing test rig, as shown in Figure 11. The test bench mainly comprises a bearing housing, a radial loader, a tachometer-torque meter, and a motor. Its drive system includes a 7.5 kW variable-frequency motor (speed range: 0–3000 r/min) and a 380 V, 10 kW vector-controlled three-phase inverter. The tested rolling bearing model is 6205-2-RS, and a 1.2 kHz sampling frequency was used for the vibration signal.

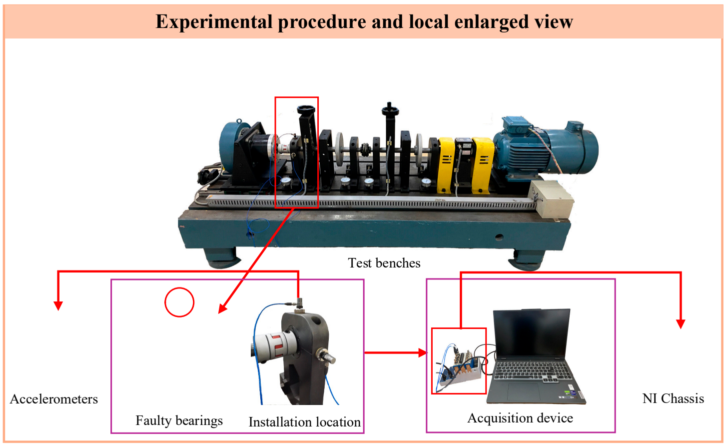

Figure 11. Experimental flow and local zoom-in diagram. The red circle indicates the localized outer-ring spall on the faulty bearing.

In the comparison between experimental and simulated responses, vibration signals from the bearing with a 0.6 mm outer-ring spall were selected and compared with the simulated signals generated by the TEHL-parameterized formulation.

4.2. Comparative Analysis of Experimental and Modeled Fault Characteristic Frequencies for an Outer-Ring Defect of 0.6 mm

A radial load of 500 N, a sampling frequency of 1.2 kHz, a rotational speed series of 1000, 1250, 1500 and 1750 rpm, and an outer-ring spalling width of 0.6 mm were configured for bearing fault experimental signal analysis. The corresponding results are illustrated in Figures 12 and 13, followed by a comparison of the theoretical, simulated, and experimental outer-ring fault characteristic frequencies under the four rotational speeds.

Figure 14 presents the envelope spectra of the outer-ring fault with a 0.6 mm spall obtained from the dynamic model at four rotational speeds: 1000, 1250, 1500, and 1750 rpm.

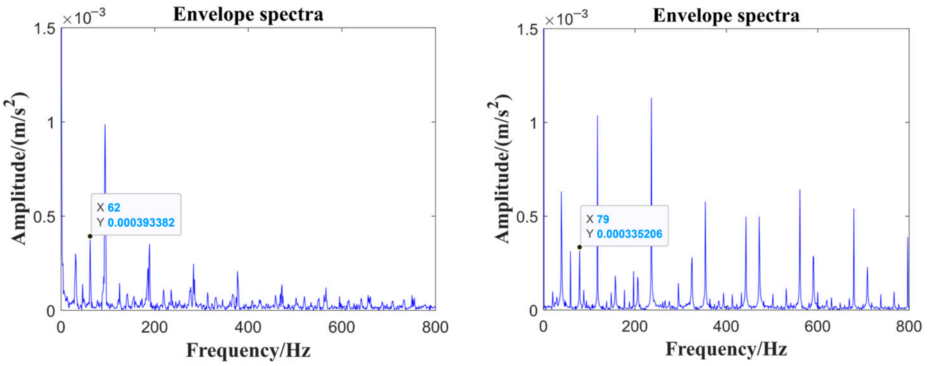

Figure 12. Experimental signals and envelope spectra for 1000 rpm and 1250 rpm outer-ring faults with a 0.6 mm spall.

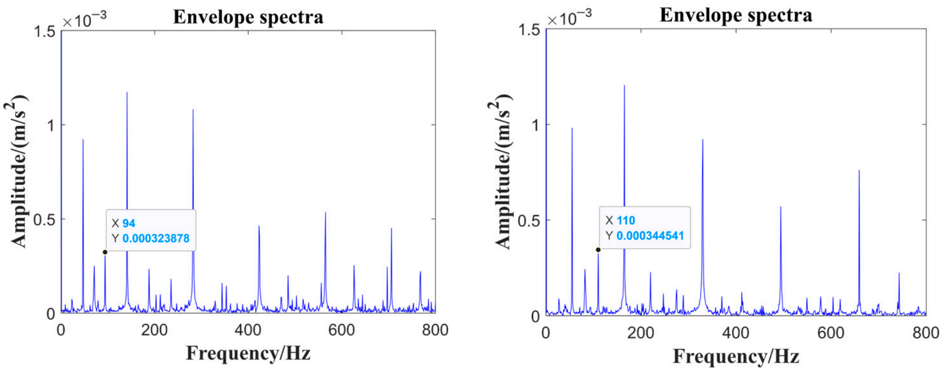

Figure 13. Signal envelope spectra for 1500 rpm and 1750 rpm outer-ring fault experiments with a 0.6 mm spall.

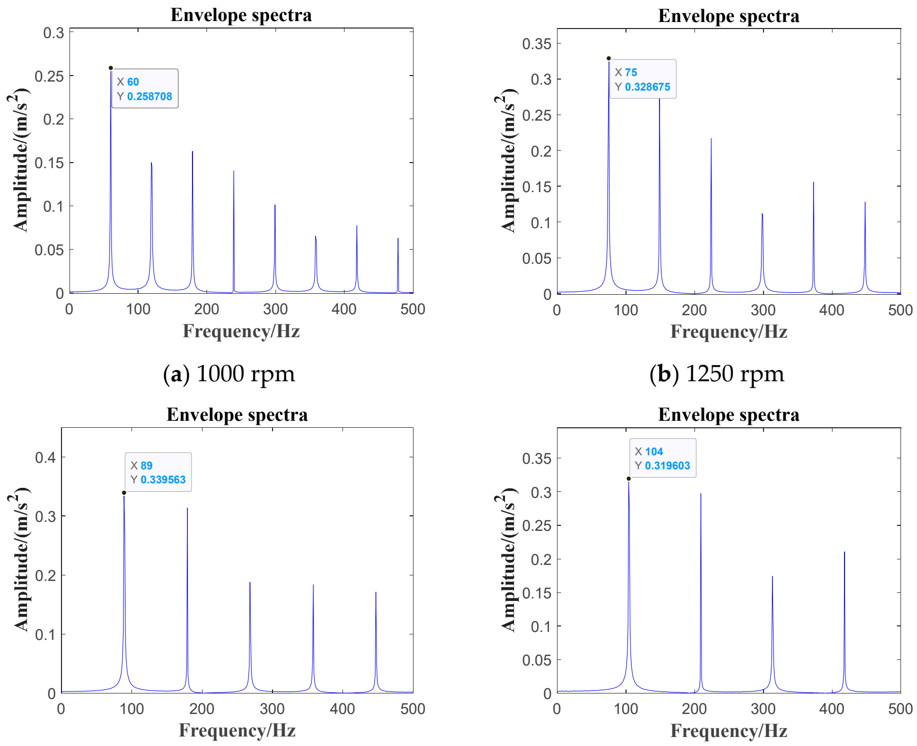

(**a**) 1000 rpm (**b**) 1250 rpm

(**c**) 1500 rpm (**d**) 1750 rpm

Figure 14. Envelope spectra of the simulated signals of 0.6 mm defects at 1000 rpm, 1250 rpm, 1500 rpm, 1750 rpm.

Based on the above results, the theoretical, simulated, and experimental outer-ring fault characteristic frequencies at different rotational speeds are compared in Table 5.

Table 5. Comparison of theoretical, simulated, and experimental outer-ring fault eigenfrequencies at different rotational speeds for 0.6 mm outer-ring faults.

Outer-Ring Failure Characteristic Frequency and Error	Rotation Speed (r/min)			
	1000	**1250**	**1500**	**1750**
Theoretical value (Hz)	59.54	74.42	89.30	104.19
Simulation value (Hz)	60	75	89	104
Experimental value (Hz)	62	79	94	110
Simulation and theoretical errors (%)	0.77	0.78	0.34	0.18
Simulation and experimental errors (%)	3.23	5.06	5.32	5.45

Through the comparative analysis of the 0.6 mm outer-ring fault eigenfrequency at four different rotational speeds of 1000 rpm, 1250 rpm, 1500 rpm and 1750 rpm in Table 5 for the theoretical, simulated, and experimental values, it can be seen that the simulation and theoretical error are within 0.78%, and the maximum error between the simulated and experimental values is 5.45%.

4.3. Quantitative Comparative Analysis of Experimental and Modeled Double Impacts with Outer-Ring Defect of 0.6 mm

In the quantitative comparative analysis of the experimental and model signals for the outer-ring spalling defect of 0.6 mm, the 1000 rpm experimental signal is selected for the double-shock quantitative analysis study. Figure 15 depicts the time-domain waveform of the experimental signal for the outer ring with a 0.6 mm fault under 1000 rpm operating condition, along with its localized time-domain magnification.

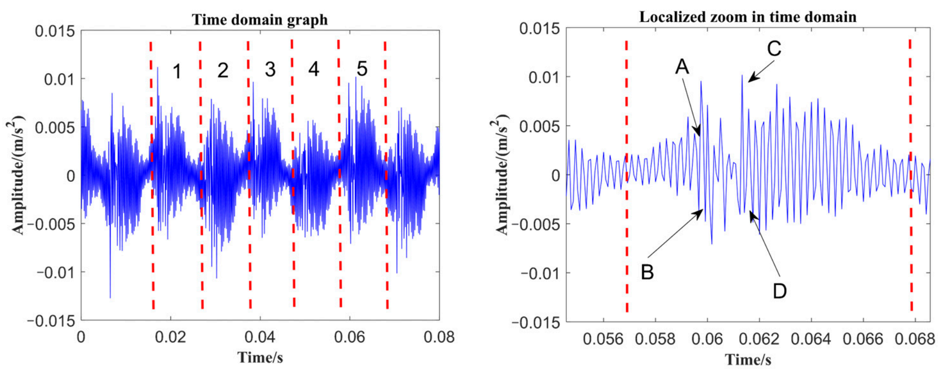

(**a**) Time-domain graph (**b**) Localized zoom in time domain

Figure 15. Time-domain plot of the experimental signal with time-domain local magnification for the 1000 rpm outer ring 0.6 mm fault.

The time-domain waveform in Figure 15a shows periodic impact responses for the bearing with a 0.6 mm outer-ring spall. The red dotted lines delimit five successive impact periods, which are labeled as 1–5. After the signal is divided into five periods, the fifth period is selected for local enlargement and characteristic-point identification, as shown in Figure 15b. In Figure 15b, points A and C are identified as the entry-impact and exit-impact instants, respectively, while points B and D denote adjacent local extrema used as auxiliary markers for double-impact identification. The double-impact time-interval quantification method based on the TEHL-parameterized formulation is then applied to estimate the outer-ring spall size. The estimated value is compared with the reference spall size of 0.6 mm, and the results are summarized in Table 6.

Table 6. Comparison between the reference 0.6 mm outer-ring spall size and the estimated spall size.

Parameter Name	Numerical Values and Units
Reference outer-ring spall size	0.6 mm
Estimated spall size by the TEHL-based method	0.665 mm
Absolute error	0.065 mm
Relative error	10.83%

As shown in Table 6, the spall size estimated by the TEHL-based quantitative diagnosis method is 0.665 mm, whereas the reference outer-ring spall size is 0.6 mm. The absolute error is 0.065 mm, corresponding to a relative error of 10.83%. This result shows that the estimated spall size is in reasonable agreement with the reference defect size under the tested conditions, supporting the applicability of the proposed TEHL-based quantitative diagnosis method for outer-ring spall-size estimation.

5. Conclusions

This paper proposes a quantitative diagnosis method for rolling bearings with outer-ring spalls. By establishing a physical transfer path from the local lubricated interface to the macroscopic double-impact response, this study bridges the gap between tribodynamics and spall-size estimation. The main conclusions are as follows:

1. A novel equivalent stiffness–damping representation is formulated to characterize the point-contact TEHL interface. Unlike conventional idealized Hertzian assumptions, this approach explicitly parameterizes the temperature-dependent oil-film pressure, film thickness, and inner–outer raceway thermal asymmetry, providing a rigorous tribological boundary for localized-defect modeling.
2. The physical mechanism of the lubricated double-impact response is elucidated by integrating the TEHL-derived representation into a classical 5-DOF framework. The model reveals that the oil film essentially acts as an additional dynamic clearance and damping buffer. This mechanism alters the spatial trajectory of rolling elements traversing the spall and induces phase delays in impact force peaks, thereby affecting the double-impact time interval.
3. The proposed method significantly improves the accuracy of spall-size quantification under thermally coupled conditions. Comparative analyses and experimental validation demonstrate that the TEHL-parameterized formulation restricts the frequency estimation error to within 5.45% and achieves a spall-size prediction error of 10.83% in experiments. Furthermore, it explicitly outperforms conventional 5-DOF, 4-DOF, and 2-DOF dry-contact models across all defect sizes (with theoretical errors reduced to below 6.00%), validating its reliability for high-precision fault diagnosis.

Author Contributions: W.J.: conceptualization, methodology, writing—original draft preparation. C.L.: investigation, data curation. T.L.: investigation, validation. J.H.: formal analysis, visualization. C.Z. (Chengshi Zhang): software, formal analysis. F.J.: resources, validation. F.Z.: methodology, supervision. C.Z. (Chao Zhang): project administration, funding acquisition, writing—review and editing. All authors have read and agreed to the published version of the manuscript.

Funding: This research was funded by the National Natural Science Foundation of China, grant number 52305115; the Natural Science Foundation of the Inner Mongolia Autonomous Region, grant number 2023QN05031; the Inner Mongolia Autonomous Region Science and Technology Special Project, grant number 2024SKYPT0032; the Science and Technology Support Project for the Construction of the National Sustainable Development Agenda Innovation Demonstration Zone, grant number KCX2024010; the Baotou Municipal Science and Technology Program, grant number 2025C1001; and the Inner Mongolia Autonomous Region Key R&D and Technology Transfer Special

Project, grant number 2025KJHZ0033. The authors also thank the State Key Laboratory of Tribology at Tsinghua University for providing experimental facilities and technical guidance.

Data Availability Statement: Due to laboratory regulations, the method of obtaining experimental data is temporarily unavailable.

Conflicts of Interest: The authors declare that they have no known competing financial interests or personal relationships that could have appeared to influence the work reported in this manuscript. All authors confirm that the research was conducted in accordance with ethical standards and that no conflicts of interest exist. The funding sources for this study are acknowledged in the Acknowledgments section, and they did not influence the design, execution, or interpretation of the research.

References

1. Zhang, C.; Liu, T.; Wang, Y.; He, H.; Zhang, C. Mechanism Study of Symmetric Mechanism-Rolling Bearing Dynamic System Considering the Influence of Temperature Factor. *Symmetry* **2023**, *15*, 2166. [CrossRef]
2. Rahnejat, H.; Gohar, R. The Vibrations of Radial Ball Bearings. *Proc. Inst. Mech. Eng. Part C J. Mech. Eng. Sci.* **1985**, *199*, 181–193. [CrossRef]
3. Wijnant, Y.H.; Wensing, J.A.; van Nijen, G.C. The Influence of Lubrication on the Dynamic Behaviour of Ball Bearings. *J. Sound Vib.* **1999**, *222*, 579–596. [CrossRef]
4. Sarangi, M.; Majumdar, B.C.; Sekhar, A.S. On the Dynamics of Elastohydrodynamic Mixed Lubricated Ball Bearings. Part I: Formulation of Stiffness and Damping Coefficients. *Proc. Inst. Mech. Eng. Part J J. Eng. Tribol.* **2005**, *219*, 411–421. [CrossRef]
5. Mohammadpour, M.; Johns-Rahnejat, P.M.; Rahnejat, H. Roller Bearing Dynamics under Transient Thermal-Mixed Non-Newtonian Elastohydrodynamic Regime of Lubrication. *Proc. Inst. Mech. Eng. Part K J. Multi-Body Dyn.* **2015**, *229*, 407–423. [CrossRef]
6. Zhang, Y.Y.; Wang, X.L.; Yan, X.L. Dynamic Behaviors of the Elastohydrodynamic Lubricated Contact for Rolling Bearings. *J. Tribol.* **2013**, *135*, 021501. [CrossRef]
7. Luo, M.; Guo, Y.; André, H.; Wu, X.; Na, J. Dynamic Modeling and Quantitative Diagnosis for Dual-Impulse Behavior of Rolling Element Bearing with a Spall on Inner Race. *Mech. Syst. Signal Process.* **2021**, *158*, 107711. [CrossRef]
8. Gomez, J.L.; Bourdon, A.; André, H.; Rémond, D. Modelling Deep Groove Ball Bearing Localized Defects Inducing Instantaneous Angular Speed Variations. *Tribol. Int.* **2016**, *98*, 270–281. [CrossRef]
9. Jiang, Y.; Huang, W.; Luo, J.; Wang, W. An Improved Dynamic Model of Defective Bearings Considering the Three-Dimensional Geometric Relationship between the Rolling Element and Defect Area. *Mech. Syst. Signal Process.* **2019**, *129*, 694–716. [CrossRef]
10. Yan, P.; Yan, C.; Wang, K.; Wang, F.; Wu, L. 5-DOF Dynamic Modeling of Rolling Bearing with Local Defect Considering Comprehensive Stiffness under Isothermal Elastohydrodynamic Lubrication. *Shock Vib.* **2020**, *2020*, 9310278. [CrossRef]
11. Tian, J.; Zhang, C.; Liang, H.; Guo, D. Simulation of the Load Reduction Process of High-Speed Angular Contact Ball Bearing with Coupling Model of Dynamics and Thermo-Elastohydrodynamic Lubrication. *Tribol. Int.* **2022**, *165*, 107292. [CrossRef]
12. Wang, Y.; Yan, C.; Lu, Z.; Liu, Y.; Wu, L. Effect of Thermal Elastohydrodynamic Lubrication on Vibration Characteristics of Ball Bearing with Local Defect. *Proc. Inst. Mech. Eng. Part K J. Multi-Body Dyn.* **2022**, *236*, 488–500. [CrossRef]
13. Tian, Y.; Yan, C.; Liu, Y.; Kang, J.; Lu, Z.; Wu, L. Dynamic Modelling of Deep Groove Ball Bearings with Different Local Defects Considering Skidding and Thermal Elastohydrodynamic Lubrication. *Proc. Inst. Mech. Eng. Part K J. Multi-Body Dyn.* **2023**, *237*, 511–533. [CrossRef]
14. Huo, Z.; Chen, J.; Hao, L.; Gao, J. Study on the Effect of Starved Lubrication on the Dynamic Characteristics of Locally Failed Roller Bearings. *Tribol. Trans.* **2024**, *67*, 952–961. [CrossRef]
15. Bai, X.; Zou, R.; Shi, H.; Zheng, H. Influence of Lubrication State Transition on Dynamic Characteristics of Deep Groove Ball Bearing with Localized Defect in Thermal Environment. *Int. J. Non-Linear Mech.* **2024**, *167*, 104879. [CrossRef]
16. Huo, Z.; Chen, J.; Hao, L.; Gao, J. Dynamic Investigation of Deep Groove Ball Bearings with Localised Failure of Outer Ring Considering the Effect of Starved Lubrication. *Lubr. Sci.* **2025**, *37*, 315–327. [CrossRef]
17. Peng, C.; Wei, J.; Liu, K.; Cao, H. Dynamic Characteristics of Angular Contact Ball Bearings with Mild Defect on Outer Raceway. *Eng. Fail. Anal.* **2025**, *178*, 109721. [CrossRef]
18. Epps, I.K. An Investigation into Vibrations Excited by Discrete Faults in Rolling Element Bearings. Ph.D. Thesis, University of Canterbury, Christchurch, New Zealand, 1991. Available online: https://ir.canterbury.ac.nz/handle/10092/6025 (accessed on 24 June 2026).

19. Randall, R.B.; Sawalhi, N. Signal Processing Tools for Tracking the Size of a Spall in a Rolling Element Bearing. In *IUTAM Symposium on Emerging Trends in Rotor Dynamics*; IUTAM Bookseries; Gupta, K., Ed.; Springer: Dordrecht, The Netherlands, 2011; Volume 25, pp. 429–440. [CrossRef]
20. Sawalhi, N.; Randall, R.B. Vibration Response of Spalled Rolling Element Bearings: Observations, Simulations and Signal Processing Techniques to Track the Spall Size. *Mech. Syst. Signal Process.* **2011**, *25*, 846–870. [CrossRef]
21. Ming, A.B.; Zhang, W.; Qin, Z.Y.; Chu, F.L. Dual-Impulse Response Model for the Acoustic Emission Produced by a Spall and the Size Evaluation in Rolling Element Bearings. *IEEE Trans. Ind. Electron.* **2015**, *62*, 6606–6615. [CrossRef]
22. Singh, M.; Kumar, R. Thrust Bearing Groove Race Defect Measurement by Wavelet Decomposition of Pre-Processed Vibration Signal. *Measurement* **2013**, *46*, 3508–3515. [CrossRef]
23. Jena, D.P.; Panigrahi, S.N. Precise Measurement of Defect Width in Tapered Roller Bearing Using Vibration Signal. *Measurement* **2014**, *55*, 39–50. [CrossRef]
24. He, S.; Zhu, L.; Li, H.; Hu, C.; Bao, J. Cross-Condition Quantitative Diagnosis Method for Bearing Faults Based on IDRSN-ECDAN. *Meas. Sci. Technol.* **2024**, *35*, 025129. [CrossRef]
25. Wu, R.; Wang, X.; Ni, Z.; Zeng, C. Dual-Impulse Behavior Analysis and Quantitative Diagnosis of the Raceway Fault of Rolling Bearing. *Mech. Syst. Signal Process.* **2022**, *169*, 108734. [CrossRef]
26. Luo, M.; Guo, Y.; Su, Z.; André, H.; Tang, Z.; Zhou, C.; Li, C. Defect Quantification Evaluation of a Rolling Element Bearing Based on Physical Modelling and Instantaneous Vibration Energy Investigation. *J. Sound Vib.* **2025**, *600*, 118875. [CrossRef]
27. Roelands, C.J.A.; Winer, W.O.; Wright, W.A. Correlational Aspects of the Viscosity–Temperature–Pressure Relationship of Lubricating Oils. *J. Lubr. Technol.* **1971**, *93*, 209–210. [CrossRef]
28. Houpert, L. New Results of Traction Force Calculations in Elastohydrodynamic Contacts. *J. Tribol.* **1985**, *107*, 241–245. [CrossRef]
29. Dowson, D.; Higginson, G.R. *Elastohydrodynamic Lubrication*; Pergamon Press: Oxford, UK, 1966.
30. Johnson, K.L. *Contact Mechanics*; Cambridge University Press: Cambridge, UK, 1985. [CrossRef]
31. Cheng, H.S. A Refined Solution to the Thermal-Elastohydrodynamic Lubrication of Rolling and Sliding Cylinders. *ASLE Trans.* **1965**, *8*, 397–410. [CrossRef]
32. Jaeger, J.C. Moving Sources of Heat and the Temperature at Sliding Contacts. *J. Proc. R. Soc. N. S. W.* **1943**, *76*, 203–224. [CrossRef]
33. Hertz, H. Ueber die Berührung fester elastischer Körper. *J. Reine Angew. Math.* **1882**, *92*, 156–171. [CrossRef]
34. Harris, T.A.; Kotzalas, M.N. *Essential Concepts of Bearing Technology*, 5th ed.; CRC Press: Boca Raton, FL, USA, 2006. [CrossRef]
35. Genta, G. On a Persistent Misunderstanding of the Role of Hysteretic Damping in Rotor Dynamics. *J. Vib. Acoust.* **2004**, *126*, 459–461. [CrossRef]
36. Hamrock, B.J.; Dowson, D. Elastohydrodynamic Lubrication of Elliptical Contacts for Materials of Low Elastic Modulus I—Fully Flooded Conjunction. *J. Lubr. Technol.* **1978**, *100*, 236–245. [CrossRef]
37. Aini, R.; Rahnejat, H.; Gohar, R. A Five Degrees of Freedom Analysis of Vibrations in Precision Spindles. *Int. J. Mach. Tools Manuf.* **1990**, *30*, 1–8. [CrossRef]

Disclaimer/Publisher's Note: The statements, opinions and data contained in all publications are solely those of the individual author(s) and contributor(s) and not of MDPI and/or the editor(s). MDPI and/or the editor(s) disclaim responsibility for any injury to people or property resulting from any ideas, methods, instructions or products referred to in the content.